Mass Ratios in Stellar Triple Systems that Admit Horseshoe Orbits

by

Bhaskaran Balaji

Submitted to the Department of Physics in partial fulfillment of the Requirements for the Degree of

BACHELOR OF SCIENCE

at the

MASSACHUSETTS INSTITUTE OF TECHNOLOGY

June 2016

Signature of Author Signature redacted
Department of Physics
May 13, 2016

Certified by Signature redacted
Saul Rappaport
Thesis Supervisor, Department of Physics

Accepted by Signature redacted
Nergis Malvalvala
Senior Thesis Coordinator, Department of Physics

Mass Ratios in Stellar Triple Systems that Admit Horseshoe Orbits

by

Bhaskaran Balaji

Submitted to the Department of Physics
on May 18, 2016, in partial fulfillment of the
requirements for the degree of
Bachelor of Science

Abstract

We examine possible configurations of stellar triple systems that give rise to "horseshoe orbits" in the smallest body. Several configurations are tested according to the initial parameters of mass for each of three bodies and position and velocity for the smallest body. The masses are arranged hierarchically, so as to mimic systems like Sun-Jupiter-Trojan. For a mass ratio of $1{:}10^{-4}{:}10^{-8}$ known to produce horseshoe orbits, a grid search was performed on position and velocity of the small body to determine admissible initial conditions. Then, a strongly suitable initial condition was chosen to run another grid search on masses of the middle and small bodies. Choosing a criterion for stability of horseshoe orbits—given that they all decay—produced a timescale for stability, with (numerical) functional dependences on the middle and smaller masses. Fitting a power law for each resulted in exponents of $k_1 = -1.006 \pm 0.006$ and $k_2 = -1.047 \pm 0.005$ respectively, which we compare to related results from Murray & Dermott (1981a).

Thesis Supervisor: Saul Rappaport
Title: Professor of Physics, Emeritus

Acknowledgments

The author would like to thank Prof. Rappaport for his guidance regarding the work in this thesis, as well as in the production of the thesis itself.

Contents

List of Figures

Chapter 1

Introduction

The three-body problem—that is, the problem of determining the motions of three masses according to their mutual gravitational attraction—has been an object of physical and mathematical interest for centuries. While the corresponding two-body problem (the "Kepler problem") is analytically and generally solved, and has in fact become a standard part of physics curricula, the same cannot be said of the three-body problem. Instead, progress has been made by imposing certain simplifying conditions on the system.

For example, the case in which two of the bodies move in fixed, circular orbits according to the two-body problem and the third body is of negligible mass (and thus exerts a negligible gravitational force) is known as the *circular, restricted three-body problem.* In this thesis, we first consider in particular conditions of a system that would satisfy the "circular" and "restricted" (negligible third mass) criteria, in order to derive analytic solutions for orbits. Later, we shed the "restriction" but perform numerical calculations in a system that remains close to circular.

1.1 Motivation for Studying Horseshoe Orbits

There are several types of motion that have been observed to be possible for the third body in real systems that are well approximated by the circular, restricted three-body problem. The most prominent are those known as Trojan (or tadpole) orbits

and horseshoe orbits, the former of which has hundreds, if not thousands, of examples in the Solar System; and the latter of which has several (e.g. Christou & Asher 2011, Dermott & Murray 1981b). The descriptive names reflect the shapes that the orbits appear to trace out in the rotating frame of reference in which the two larger masses are fixed.

Not all pairs of larger masses admit such orbits, however. In the case of Trojans, an analytic solution of the motion of a small tertiary particle determines that only certain ratios between the two larger masses admit stable orbits of the third. We will reproduce this solution here for the sake of comparison.

However, similar constraints have not been found for horseshoe orbits with a *massive* third body. In this paper, we seek to supply such constraints by running numerical simulations on a range of three-body configurations, sufficiently finely sampled in parameter space.

Chapter 2

Mathematical Background

We first describe the method and results for solving the Trojan problem, as we will refer to it for comparison with the horseshoe case. This requires a preliminary explanation of the Lagrange points.

2.1 Triangular Lagrange Points

We first derive, as in Murray & Dermott (1999), the locations of the L4 and L5 points of a system of two massive bodies in circular orbit. Our assumptions and variables are as follows:

1. There are two massive bodies, $m_1 > m_2$, with $m_1 + m_2 = 1$.

2. We operate in two dimensions, with $\hat{x}$ pointing from m_1 to m_2 (and $\hat{y}$ 90° counterclockwise). This is therefore the rotating frame of the binary orbit.

3. The origin is placed at the center of mass; that is, $m_1 x_1 + m_2 x_2 = 0$, and we set the distance between the two masses $x_2 - x_1 = 1$, so that $x_1 = -m_2$ and $x_2 = m_1$.

4. While x and y are the coordinates of a test particle, r_1 and r_2 are the distances from that particle to m_1 and m_2, respectively.

Because we are in the rotating frame of reference, the total "pseudo-potential" U, known as the Roche potential, is the sum of the gravitational and centrifugal potentials:

$$U = \frac{m_1}{r_1} + \frac{m_2}{r_2} + \frac{1}{2}\left(x^2 + y^2\right) \tag{2.1}$$

We may instead have set U as $-U$, but the only calculation we are interested in sets $\nabla U = 0$, so the two cases are equivalent in this respect.

Given the definitions of r_1 and r_2, as well as the locations of m_1 and m_2, we have

$$m_1 r_1^2 + m_2 r_2^2 = x^2 + y^2 + m_1 m_2 \tag{2.2}$$

from which we may rewrite

$$U = m_1\left(\frac{1}{r_1} + \frac{r_1^2}{2}\right) + m_2\left(\frac{1}{r_2} + \frac{r_2^2}{2}\right) - \frac{1}{2}m_1 m_2 \tag{2.3}$$

The Lagrange points are defined as those points in the rotating frame of the binary at which a particle would remain stationary. Thus, we seek the local extrema of the Roche potential, where $\nabla U = 0$:

$$\frac{\partial U}{\partial x} = \frac{\partial U}{\partial r_1}\frac{\partial r_1}{\partial x} + \frac{\partial U}{\partial r_2}\frac{\partial r_2}{\partial x} = 0 \tag{2.4}$$

$$\frac{\partial U}{\partial y} = \frac{\partial U}{\partial r_1}\frac{\partial r_1}{\partial y} + \frac{\partial U}{\partial r_2}\frac{\partial r_2}{\partial y} = 0 \tag{2.5}$$

By inspection, these equations have the simultaneous solution

$$\frac{\partial U}{\partial r_1} = \frac{\partial U}{\partial r_2} = 0 \tag{2.6}$$

Evaluating these partial derivatives, we have

$$m_1\left(r_1 - \frac{1}{r_1^2}\right) = m_2\left(r_2 - \frac{1}{r_2^2}\right) = 0 \tag{2.7}$$

which results in

$$r_1 = r_2 = 1 \tag{2.8}$$

We now understand the description "triangular" for the L4 and L5 points: they are the two points in the plane that form equilateral triangles with the locations of the two massive bodies.

The remaining Lagrange points (L1, L2, and L3) fall along the x-axis, as in Figure 2-1, with L3 near the antipodal point to m_2 along its orbit around m_1. However, we will focus here on motion around L4 and L5.

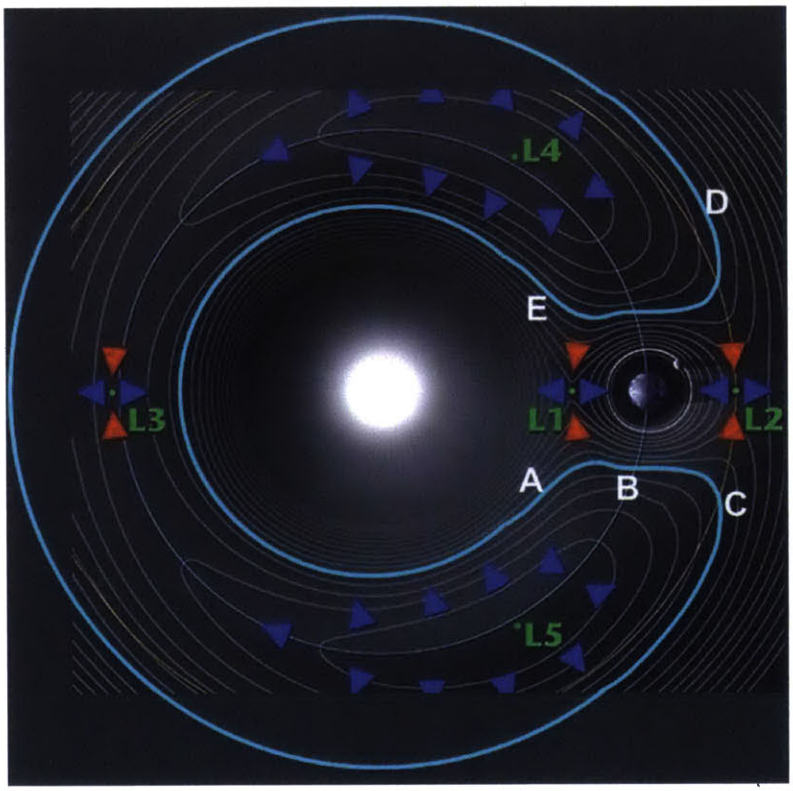

Figure 2-1: The Roche potential as a contour plot for the Sun-Earth system (not to scale, and with the Moon also drawn) with the Lagrange points labeled. L4 and L5 are local maxima, while L1, L2, L3 are saddle points. Also noted are the signs of the directional gradients near the Lagrange points, as well as an example of a horseshoe orbit (light blue), with points A, B, C, D, E indicating a possible direction of motion. (Image public domain, adapted from NASA.)

2.2 Trojan Orbits

We now establish the mass-ratio stability criterion for the "Trojan" orbits around the L4 and L5 points, following solutions to the problem on an MIT graduate exam (Rappaport 2006). Remarkably, although the Roche potential is at a local maximum at L4 and L5, there exist stable orbits around those points, as we will demonstrate.

We begin with a Taylor expansion of the dimensionless Roche potential ϕ near the L4 point, with ξ and η displacements in the x and y directions, respectively, and μ defined as

$$\mu = \frac{m_1 - m_2}{m_1 + m_2} \tag{2.9}$$

so that

$$\phi \simeq \frac{3}{8}\xi^2 + \frac{9}{8}\eta^2 + \frac{3\sqrt{3}\mu}{4}\xi\eta \tag{2.10}$$

Adding the Coriolis force to the standard force, we find the total force per unit mass

$$\vec{f} = \vec{\nabla}U + 2\vec{\Omega} \times \left(\frac{d\vec{r}}{dt}\right) \tag{2.11}$$

where $\vec{\Omega}$ is the angular velocity of the rotating frame, which we assume equal to $\hat{z}$ (i.e. an angular speed of 1), and $\vec{r} = (\xi, \eta)$. This gives us the coupled equations of motion

$$\ddot{\xi} = \frac{3}{4}\xi + \frac{3\sqrt{3}\mu}{4}\eta + 2\dot{\eta} \tag{2.12}$$

$$\ddot{\eta} = \frac{9}{4}\eta + \frac{3\sqrt{3}\mu}{4}\xi - 2\dot{\xi} \tag{2.13}$$

We then substitute ansatz solutions

$$\xi = Re[Ae^{i\omega t}] \tag{2.14}$$

$$\eta = Re[Be^{i\omega t}] \tag{2.15}$$

which yield

$$-A\left(\omega^2 = \frac{3}{4}\right) = B\left(2i\omega + \frac{3\sqrt{3}\mu}{4}\right) \tag{2.16}$$

$$-B\left(\omega^2 + \frac{9}{4}\right) = A\left(-2i\omega + \frac{3\sqrt{3}\mu}{4}\right) \tag{2.17}$$

The allowed values of ω for this orbit are given by

$$\omega^4 - \omega^2 + \frac{27}{16}(1-\mu^2) = 0 \tag{2.18}$$

implying that

$$\omega^2 = \frac{1}{2} \pm \frac{1}{2}\sqrt{1 - \frac{27}{4}(1-\mu^2)} = 0 \tag{2.19}$$

Since we require stable orbits, $i\omega t$ must be purely imaginary, so ω must be purely real. This means that ω^2 must be positive; in particular,

$$\sqrt{1 - \frac{27}{4}(1-\mu^2)} > 0 \tag{2.20}$$

$$1 > \frac{27}{4}(1-\mu^2) \tag{2.21}$$

$$\mu > \sqrt{\frac{23}{27}} \tag{2.22}$$

Given the definition of μ in Equation 2.9, this gives us a lower bound on the mass ratios m_2/m_1 that admit Trojan orbits:

$$\frac{m_2}{m_1} < \frac{1-\sqrt{23/27}}{1+\sqrt{23/27}} \simeq 0.04 \tag{2.23}$$

Furthermore, we can use Equation 2.19 to estimate the periods relevant to Trojan

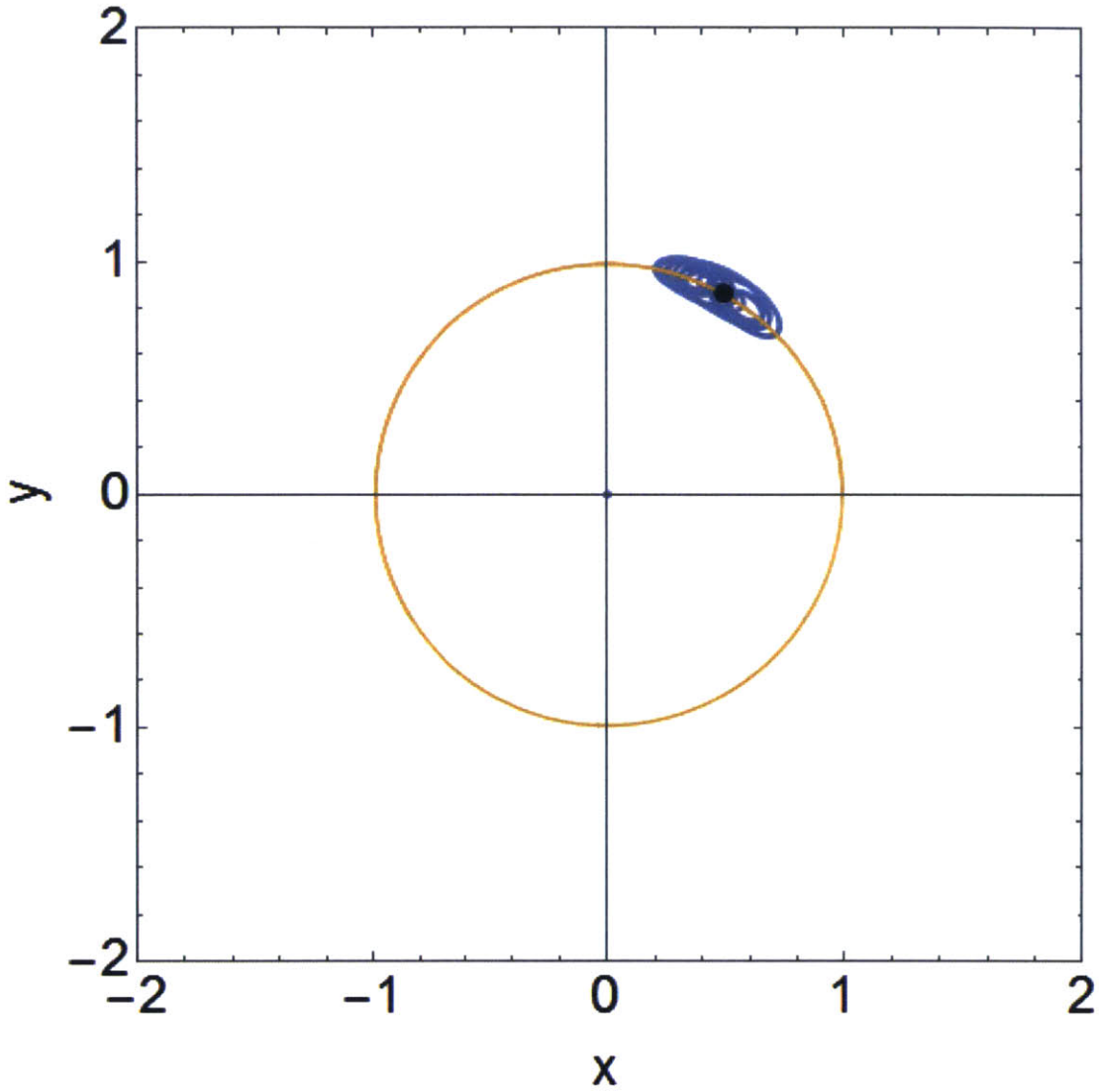

Figure 2-2: An example of a tadpole orbit in the rotating reference frame over 100 periods of the larger binary orbit (of m_2 and m_1), in blue, where $m_2/m_1 = 0.01$. The binary orbit in the non-rotating frame is also superimposed (orange), to guide the eye. The L4 point, around which the tadpole orbit librates, is indicated in black.

orbits. Assuming m_2 is small, we have $\mu \lesssim 1$, so we find two periods:

$$\omega_1^2 \simeq \frac{1}{2} + \frac{1}{2}\left(1 - \frac{27}{8}(1-\mu^2)\right) = 1 - \frac{27}{16}(1-\mu^2) \tag{2.24}$$

$$\omega_1 \simeq 1 - \frac{27}{32}(1-\mu^2) \lesssim 1 \tag{2.25}$$

$$\omega_2^2 \simeq \frac{1}{2} - \frac{1}{2}\left(1 - \frac{27}{8}(1-\mu^2)\right) = \frac{27}{16}(1-\mu^2) \tag{2.26}$$

$$\omega_2 \simeq \frac{3\sqrt{3}}{4}\sqrt{1-\mu^2} \tag{2.27}$$

ω_1 corresponds to a shorter "epicyclic" period of about 2π, similar to the binary period, while ω_2 corresponds to a longer period of the motion of the guiding center of the Trojan orbit around the Lagrange point.

Figure 2-2 shows an example of a Trojan orbit, for a system in which $m_2/m_1 = 0.01$.

With this result, we can now understand the motivation for examining the effect of similar mass ratios on the stability of *horseshoe* orbits. As horseshoe orbits and Trojan (tadpole) orbits qualitatively look related—in the sense that a horseshoe orbit looks like a "stretched-out" tadpole orbit that extends past L3, and at certain times (while near L4 and L5) even looks locally similar to a tadpole orbit—it is reasonable to expect that the former might obey similar constraints to those of the latter.

As described in Ćuk et al. (2012), there is a similar critical mass ratio of $m_2/m_1 \approx 1/1200$ for horseshoe orbits to be stable. However, until this point we have been discussing orbits of a tertiary object with negligible mass; we would like to investigate what happens with a larger third object, although we will check our result against this bound.

Chapter 3

Numerical Simulation

The bulk of our numerical simulation was completed in two steps:

1. Given an extreme mass ratio strongly expected to produce a wide range of horseshoe orbits, we performed a numerical integration on systems with several different initial conditions for the third body nearby a parameter set known to produce a horseshoe orbit. We then selected one of the initial parameter sets resulting in the longest-lived horseshoe orbits to use in the second step.

2. Using a fixed initial position and velocity for the third mass, we similarly tested the horseshoe orbit's lifetime for many different masses of the second and third bodies (with respect to that of the first).

We next explain these two steps further, beginning with our basic integration routine.

3.1 Integration Routine

All of the following was programmed in Wolfram Mathematica.

The total mass of the system was set to 1, with the masses in decreasing order m_1, m_2, and m_t (the latter being the small "test mass"). m_1 and m_2 were given the

initial conditions in two dimensions and at $t = 0$

$$\mathbf{x_1} = (-m_2, 0)$$
$$\mathbf{v_1} = (0, -m_2)$$
$$\mathbf{x_2} = (m_1, 0)$$
$$\mathbf{v_2} = (0, m_1)$$

so that they would move in circular orbits around their common center of mass. The four quantities m_2, m_t/m_2, $|x_t| / |x_2|$, and $|v_t| / |v_2|$ were passed as parameters to the routine, and we explain in the next section how the initial conditions for $\mathbf{x_t}$ and $\mathbf{v_t}$ were determined.

Given the masses and initial conditions, the coupled differential equations for the motions of the three masses under their mutual gravitational influence were identified in a dimensionless form:

$$\frac{d^2\mathbf{x_1}}{dt^2} = -\frac{m_2\left(\mathbf{x_1} - \mathbf{x_2}\right)}{\left|\mathbf{x_1} - \mathbf{x_2}\right|^3} - \frac{m_t\left(\mathbf{x_1} - \mathbf{x_t}\right)}{\left|\mathbf{x_1} - \mathbf{x_t}\right|^3} \tag{3.1}$$

$$\frac{d^2\mathbf{x_2}}{dt^2} = -\frac{m_1\left(\mathbf{x_2} - \mathbf{x_1}\right)}{\left|\mathbf{x_2} - \mathbf{x_1}\right|^3} - \frac{m_t\left(\mathbf{x_2} - \mathbf{x_t}\right)}{\left|\mathbf{x_2} - \mathbf{x_t}\right|^3} \tag{3.2}$$

$$\frac{d^2\mathbf{x_t}}{dt^2} = -\frac{m_1\left(\mathbf{x_t} - \mathbf{x_1}\right)}{\left|\mathbf{x_t} - \mathbf{x_1}\right|^3} - \frac{m_2\left(\mathbf{x_t} - \mathbf{x_2}\right)}{\left|\mathbf{x_t} - \mathbf{x_2}\right|^3} \tag{3.3}$$

These were numerically solved until $t = t_{max}$ (also a parameter we supplied) using Mathematica's NDSolve method, which internally selects both integration methods and step sizes to optimize solution accuracy. Calculations were performed to machine precision.

By default, NDSolve chooses the integration method to use, although it does not indicate this to the user—the procedure is "under the hood." For time integration, as in our routine, the possible classes of integration methods are the following, taken from the Mathematica 10.4 documentation (Wolfram 2016):

- "Adams: predictor-corrector Adams method with orders 1 through 12"

- "BDF: implicit backward differentiation formulas with orders 1 through 5"
- "ExplicitRungeKutta: adaptive embedded pairs of 2(1) through 9(8) Runge-Kutta methods"
- "ImplicitRungeKutta: families of arbitrary-order implicit Runge-Kutta methods"
- "SymplecticPartitionedRungeKutta: interleaved Runge-Kutta methods for separable Hamiltonian systems"

NDSolve does admit the option to restrict the possible methods used. However, restricting to the "ExplicitRungeKutta" option, for example, produced no qualitative difference in the solutions. Furthermore, the total energy and angular momentum of the three-body system were no better conserved (at the same working precision) by restricting the methods NDSolve could use, generally doing so to about a part in 10^{10} in both cases. Thus, for all of our integrations seeking physical results, we did not restrict the integration methods internal to NDSolve that Mathematica used, only asking for precision in the integrated motion to 12 digits, according to Mathematica's error estimates attached to its integration methods.

The solutions for $t \in (0, t_{max})$ are saved as InterpolatingFunctions, which may be evaluated at any point within the interval $(0, t_{max})$. As such pointwise evaluation is their only use, they may be treated as packaged series of points as determined by the numerical integration done by NDSolve.

At each integration time, the angle that the binary of larger masses has rotated through is determined by measuring the position of m_2, and this angle is then used to reposition all three masses into the rotating reference frame—that is, where m_1 and m_2 remain at their initial conditions. This is done to preserve generality, although we know that for small secondary and tertiary bodies the binary orbit has an angular frequency of $\sim$1.

The horseshoe lifetime for a particular integration is defined as the first time within the interval $(0, t_{max})$ at which the third body is 10% farther from the system's

center of mass than when it started. This number is somewhat arbitrary, but it was chosen after inspection of when several different trial integrations saw their horseshoe orbits decay into non-horseshoe motions. Examples of a successful horseshoe and a decayed horseshoe are presented in Figures 3-1 and 3-2.

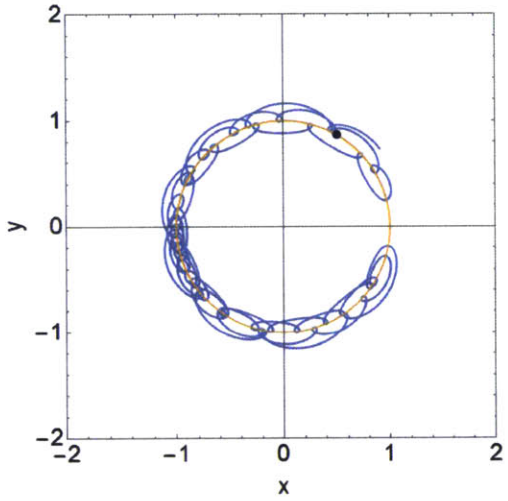

Figure 3-1: An example of a horseshoe orbit which evidently remains stable over the duration of the integration. Again, the binary orbit and L4 point are drawn for guidance. One may notice that the third body spends much of its time near L3 as opposed to near L4 or L5.

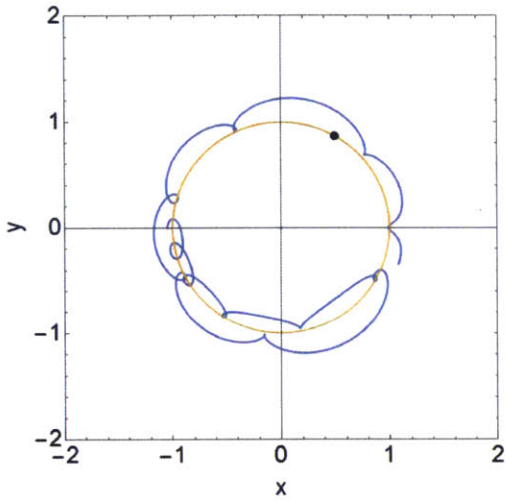

Figure 3-2: An example of a horseshoe orbit that has decayed at some point, to fall out of the horseshoe pattern. While we do not demonstrate this, if this integration is carried further, it is evident that it never again reaches a horseshoe shape once it has decayed.

Importantly, in all cases of decay, the transformation of the horseshoe orbit into a distinctly non-horseshoe shape was coupled with a general expansion (an "unraveling") of the orbit in the rotating frame, which led to our choice of this discrete decay condition. This behavior is also discussed in Dermott & Murray (1981a) and was used to calculate their lifetime estimate for horseshoe orbits (see Equation 4.1).

Furthermore, through many simulations, it was never the case that once a horseshoe orbit decayed, it ever returned to a horseshoe configuration at any later time. We did not prove this fact; however, it both was supported by the evidence from the simulations and was an intuitive assumption.

We also notice that, just as in the Trojan case, there appear to be two periods

relevant to the horseshoe orbit: an "epicyclic" period of about 2π (again similar to the binary period); and a period of motion around the horseshoe which depends significantly on the mass ratio m_2/m_1 and may be anything from tens of binary orbits to hundreds or even more. In general it seems that this longer period may be larger than in the Trojan case—as may be expected by the larger spatial expanse of the horseshoe orbit.

3.2 Step 1: Determination of Ideal Initial Conditions

By analogy to the Trojan case, we expected systems with large mass ratios m_1/m_2 to admit horseshoe orbits more readily. Thus, to determine the dependence of horseshoe lifetime on initial parameters, we first fixed m_1/m_2 and m_2/m_t both to be very large, specifically 10^4.

It was not feasible to test a full range of third-body initial conditions with positions and velocities distributed around the orbit of m_2 around m_1 (because of the large value of m_1/m_2, it is in fact meaningful to say that m_2 orbits m_1). However, according to the Uniqueness and Existence Theorems for solutions of differential equations, and given the fact that we expected to see *horseshoe orbits*, which all cross within or near a certain region in parameter space at some point in time, it would suffice to choose some point along a typical horseshoe orbit and test many initial conditions close by. We chose to test near the antipodal point of m_2's orbit around m_1, as horseshoe orbits in general should cross near this point $(-m_1, 0)$ with velocity near $(0, -m_1)$, and furthermore, this is a property that qualitatively distinguishes them from tadpole orbits. Figure 3-3 contains the results of this search, summarized in a contour plot of horseshoe lifetime as a function of the initial conditions of the third body $|x_t| \,/\, |x_2|$ and $|v_t| \,/\, |v_2|$. In terms of these conditions

$$\mathbf{x_0} \equiv \mathbf{x_t}(0) = \frac{|x_t|}{|x_2|}(-m_1, 0) \tag{3.4}$$

$$\mathbf{v_0} \equiv \mathbf{v_t}(0) = \frac{|v_t|}{|v_2|}(0, -m_1) \tag{3.5}$$

The plot may be partitioned into two regions of initial conditions that admit relatively stable orbits: a straight line with slope close to -1 and a wedge with $|v_0| \gtrsim |x_0|$. The initial conditions falling within the wedge do not produce horseshoe orbits, while those falling within the central line do. This is checked by simply integrating from sets of initial conditions sampled from among those regions; an example of a stable orbit propagated from initial conditions in the wedge is in Figure 3-4.

We summarized the central line with a linear fit as follows:

1. All points above the line $|v_0| + |x_0| = 2.05$ were eliminated, with this cut somewhat arbitrarily chosen to preserve the central line while eliminating the wedge above.

2. All points that resulted in lifetimes less than $t_{max} = 1000$ were eliminated.

3. All points at each value of x_0 were combined by averaging their v_0 values.

4. This final set of points was fit to a line, $v_0 = a\,(x_0) + b$, resulting in $a \approx -0.88$, $b \approx 1.87$. This fit is displayed in Figure 3-5.

We used this band of initial conditions that readily admitted horseshoe orbits to fix specific initial conditions (choosing some x_0 along the line and determining the corresponding v_0) and thereby test next the dependence of orbits' stability on mass ratios.

3.3 Step 2: Determination of Dependence of Stability on Mass Ratios

The basic structure and goal for this section—and indeed the project as a whole—was a grid search on masses of the secondary and tertiary bodies (with respect to that of the first, largest one). For all following integrations, we chose $|x_t| \,/\, |x_2| = 1.01$, which determined $\mathbf{x_0}$ directly and $\mathbf{v_0}$ according to the line fit described in the previous section. Given this specific set of initial conditions, we then integrated in general to

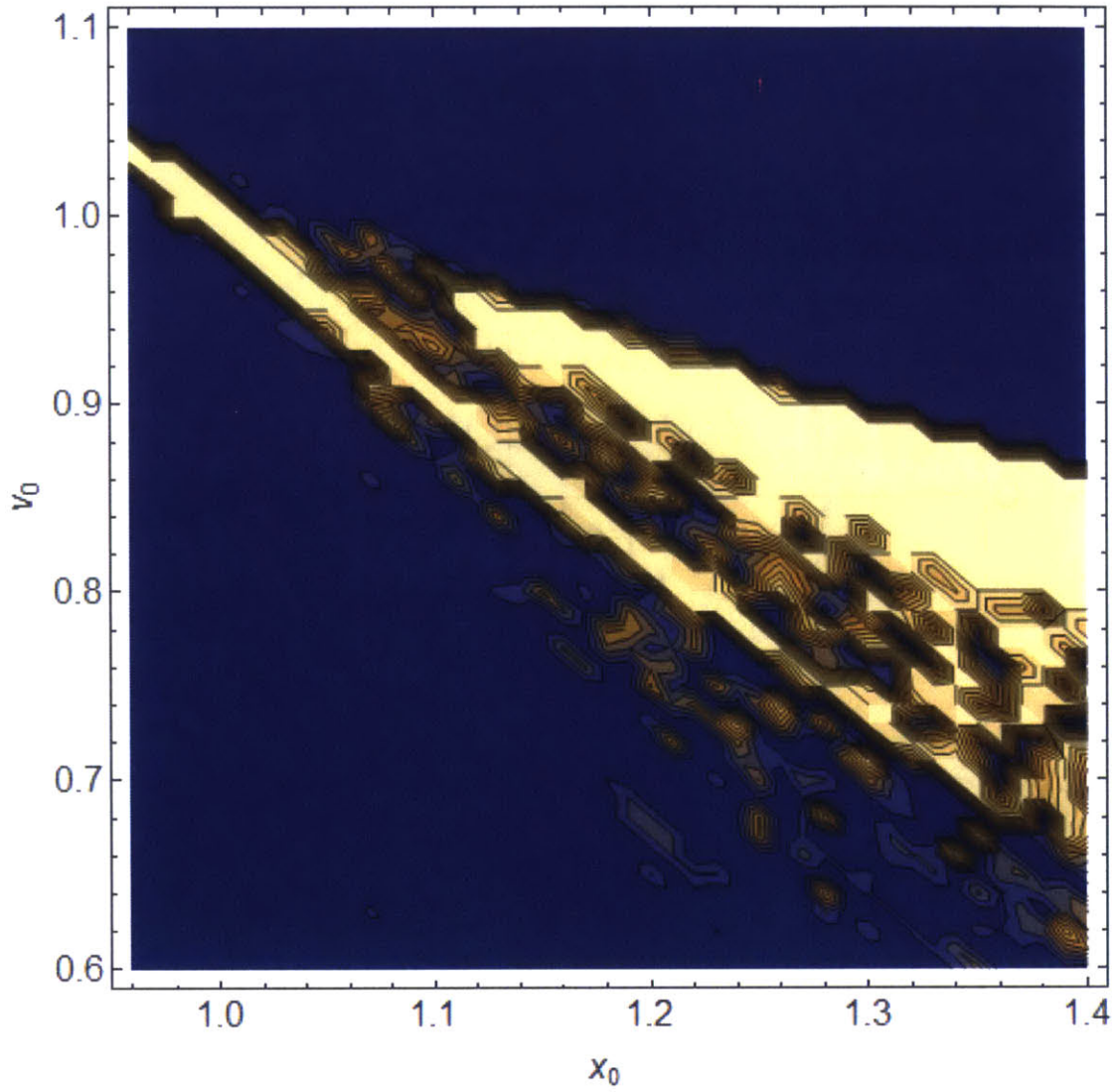

Figure 3-3: A grid search on initial positions and velocities of m_t, as described in Eqns. 3.4 and 3.5, with $m_t/m_2 = m_2/m_1 = 10^{-4}$. Contours again indicate lifetimes τ, stepped by $\Delta\tau = 100$, with blue indicating $\tau < 100$ and beige indicating $\tau \geq 1000$. Apparent discontinuities in the contours are nothing more than a shortcoming of Mathematica's rendering of the plot.

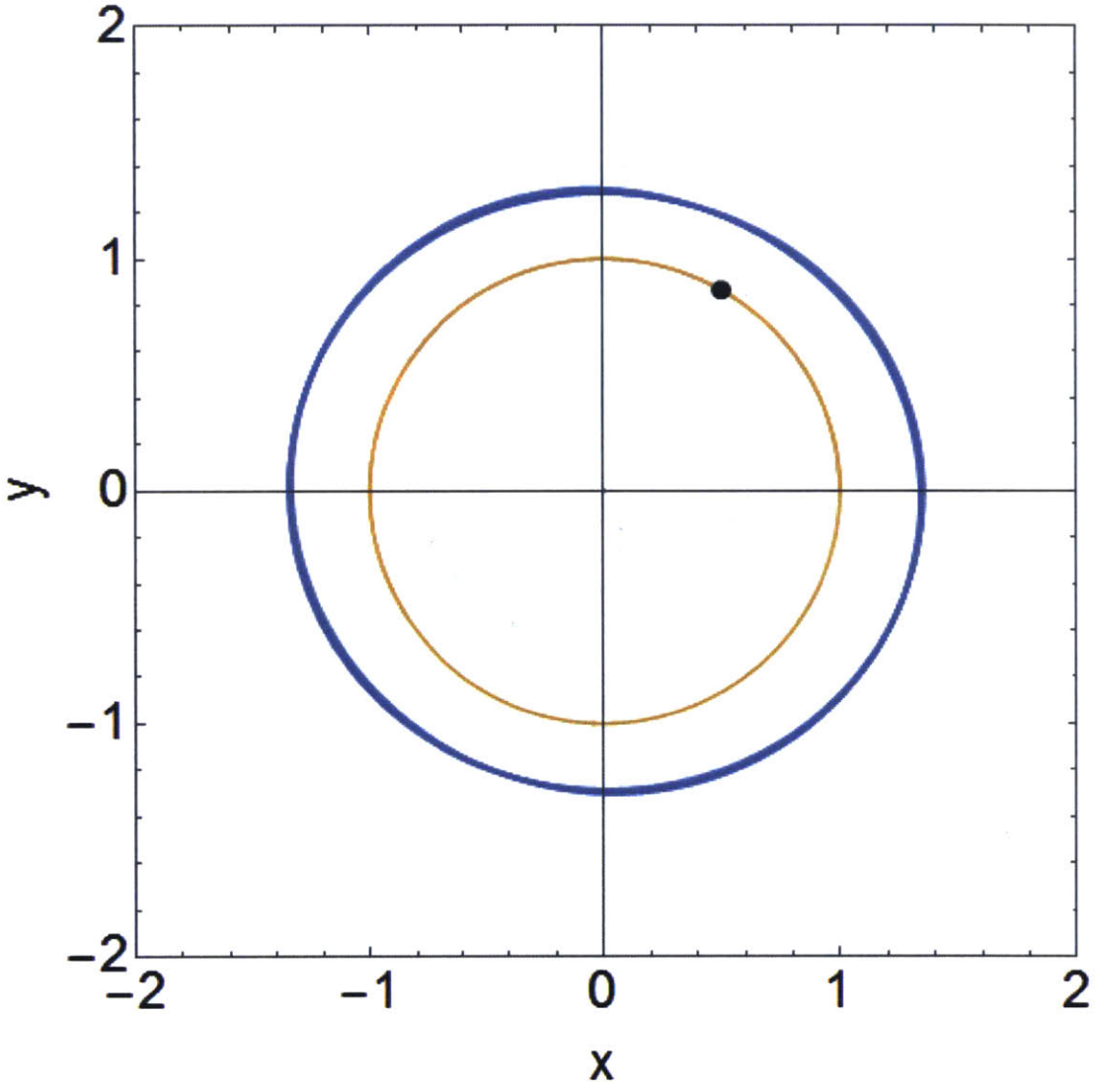

Figure 3-4: An example orbit (blue) of the third body, with initial conditions taken from the wedge in Fig. 3-3. This is just an example of such an orbit, but in general, no initial conditions taken from the wedge produce horseshoe orbits. (See Fig. 3-1 for an example of initial conditions from the central band in Fig. 3-3 which produce a horseshoe orbit.)

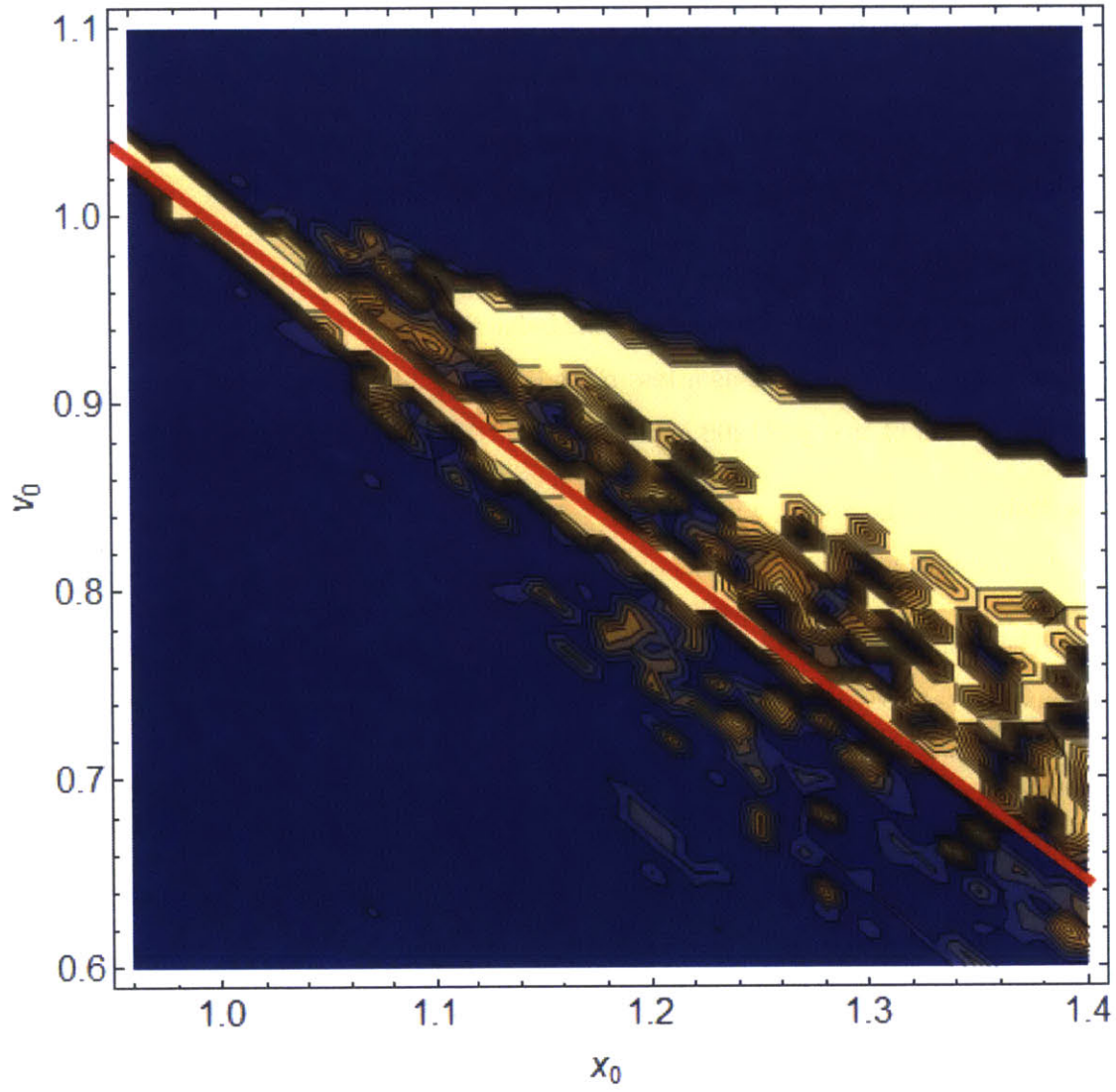

Figure 3-5: A reproduction of Fig. 3-3, but with the best-fit line (red) superimposed over the central band of successful initial parameters.

$t_{max} = 10000$ and tested the stability of the orbit for each pair $(m_2/m_1, m_t/m_2)$—which we will abbreviate as (m_2, μ_t)—with various ranges and grid spacings. Since we did not have unlimited processing power, broader searches had to be coarser to compensate.

An initial "survey" search served to direct further searches by providing us a qualitative view of different regimes in the m_2–μ_t plane. This search is displayed in Figure 3-6.

We may summarize some of the features of this search as follows:

- For $\log(m_t/m_2) = \log \mu_t \lesssim -2$ and $\log m_2 \gtrsim -3$, stability does not seem to depend on μ_t. An explanation for this behavior may be simply that in this region of μ_t, m_t truly behaves as a test mass (of negligible mass), thereby making the restriction of $m_2 \lesssim 1/1200$ as in Ćuk et al. (2012) applicable.

- Related to the above, where $\log \mu_t \lesssim -2$, there appears to exist a sharp increase in stability as $\log m_2$ decreases below -3.

- Above the $\log \mu_t = -2$ threshold, until the two smaller bodies are of comparable mass, stability of the horseshoe orbit has a dependence on not just one or the other, but both of m_2 and m_t together.

- All of the above remain true if the integrations are taken to $t_{max} > 1000$, up to $t_{max} = 10000$; this search does not appear qualitatively different for higher timescales timescales. This means that our results with $t_{max} = 10000$ in the next section—where we zoom in on an interesting region of parameter space—should similarly describe the system for even larger timescales and are thus a good proxy for generality. For an example, see Figure 3-7.

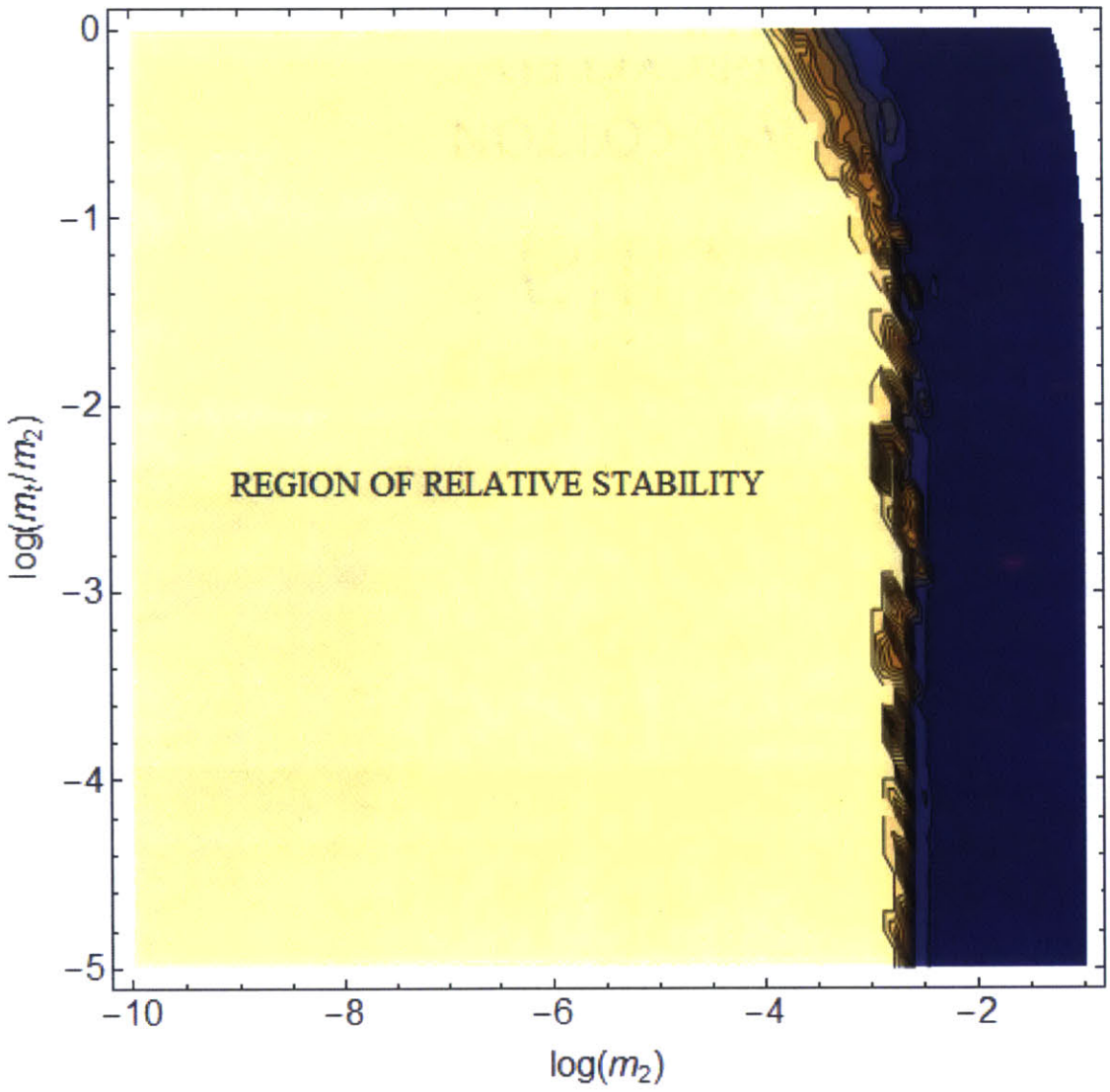

Figure 3-6: A wide "survey" search on mass ratios. Contours demarcate lifetimes τ stepped by $\Delta\tau = 100$, where blue indicates $\tau < 100$ and beige indicates $\tau \geq 1000$. For this initial survey, we integrated only to $t_{max} = 1000$. Recall that the binary period is by comparison 2π.

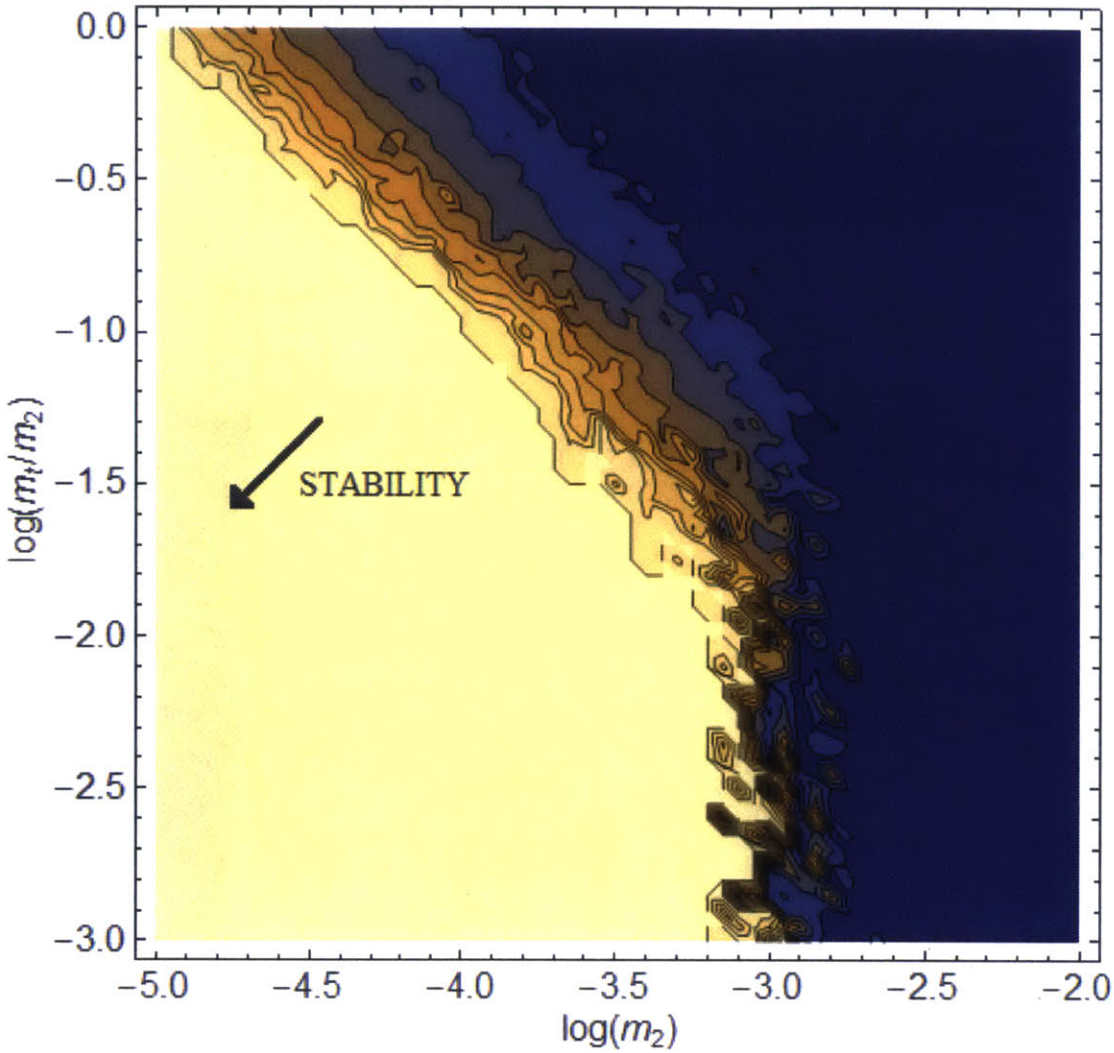

Figure 3-7: An example stability plot similar to Fig. 3-6, but zoomed in and with integration taken to $t_{max} = 10000$. Thus, contours are stepped by $\Delta\tau = 1000$, the blue region has $\tau < 1000$, and the beige has $\tau \geq 10000$. Importantly, this plot reveals effectively the same behavior as does Fig. 3-6.

Chapter 4

Analysis of Mass-Ratio Dependence; Conclusions

4.1 Dependence of Lifetime on Mass Ratios

We now zoom in slightly further than in Figure 3-7 and plot contours of $\log \tau$ for greater clarity, as well as for comparison with the time-scale dependence in Dermott & Murray (1981a) of

$$\tau \lesssim T/m_2^{5/3} \tag{4.1}$$

where T is the period of the binary orbit (i.e. the orbit of the two larger masses). The results are in Figure 4-1.

In order to summarize the information revealed by this plot, and also to mimic Dermott & Murray (1981a), we take vertical and horizontal slices and attempt to fit functions of the form

$$\tau = A m_2^{k_1(\mu_t)} \tag{4.2}$$

$$\tau = B \mu_t^{k_2(m_2)} \tag{4.3}$$

recalling that $\mu_t = m_t/m_2$. That is, we seek to describe the dependence of lifetime τ on each mass individually as a power law, of exponent dependent on the value of the

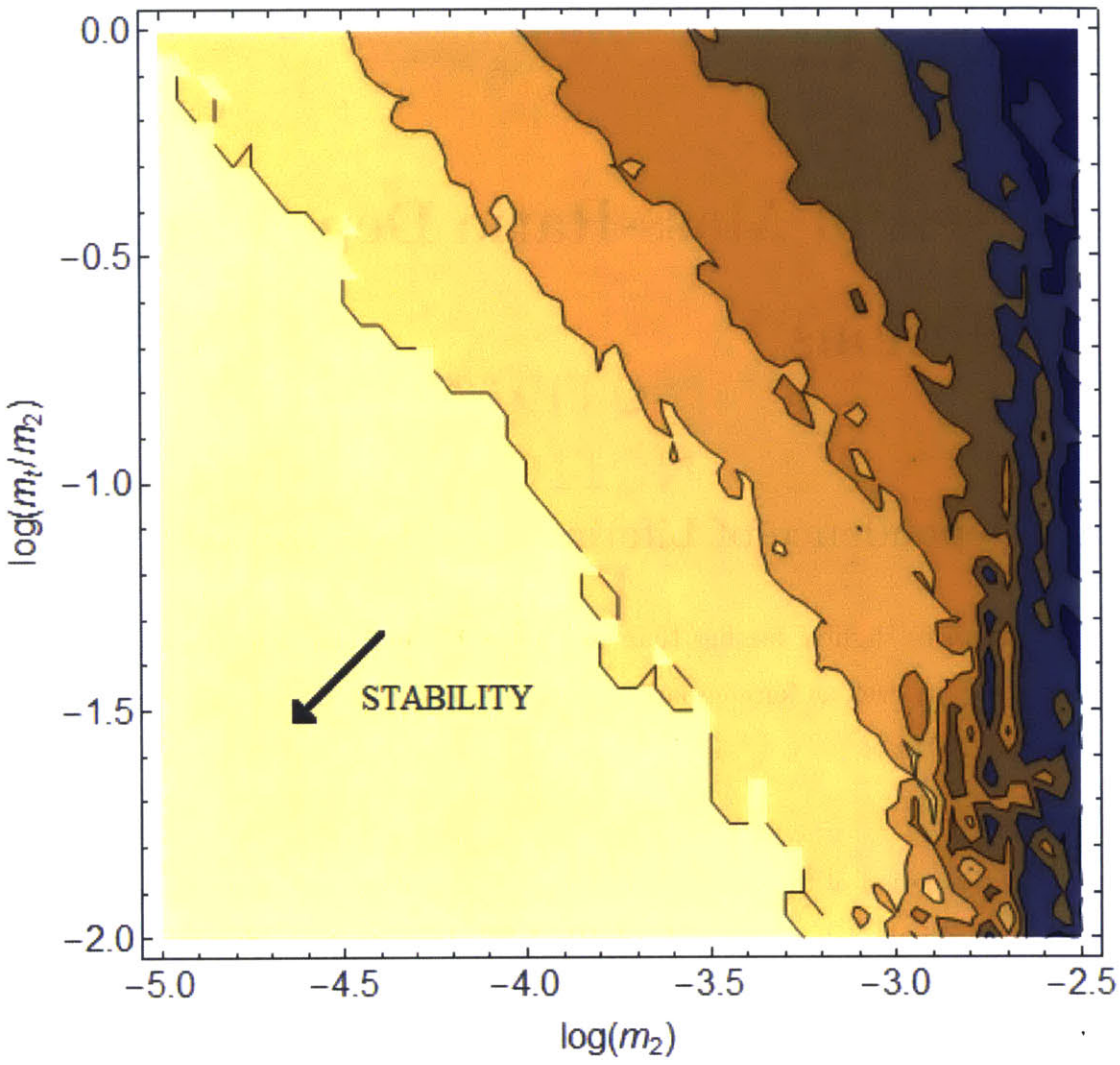

Figure 4-1: A contour plot of $\log \tau$. Here, lightest beige indicates $\log \tau \geq 4$, contours are stepped by $\Delta \log \tau = 0.5$, and so blue indicates $\log \tau < 1.5$. The plot looks somewhat messy for high m_2 and low μ_t, but for now we do not concern ourselves with this region.

other mass.

Figures 4-2 and 4-3 show examples of fitting a power law to slices of Figure 4-1. In order to perform the fit, we first identified and eliminated the points in the region that was simply limited by our integration time t_{max}, after which we fit a straight line to the remainder, to determine a slope k_1 or k_2, with error equal to the standard error associated with the fit. These measured exponents are summarized in Figures 4-4 and 4-5. One notices in the former a potentially quadratic or a constant trend, but a more clearly constant trend in the latter. To distinguish between the two in the former case would require further data and analysis; we do not thoroughly treat the quadratic possibility here.

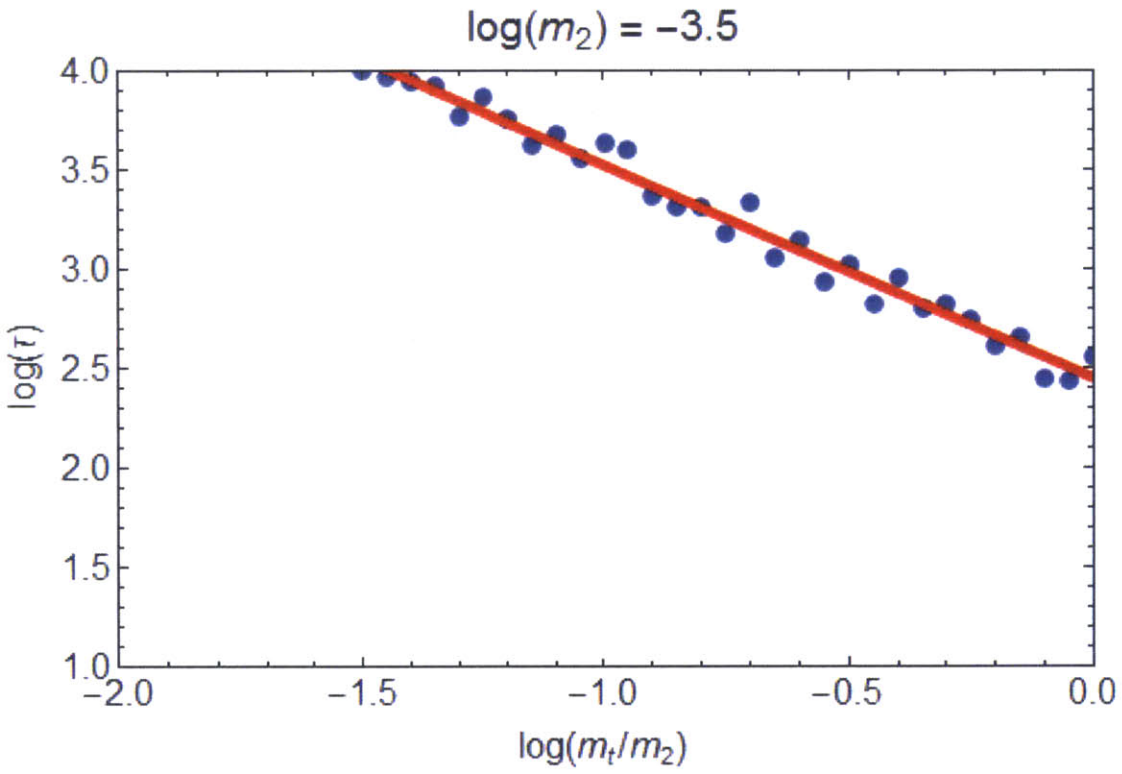

Figure 4-2: A horizontal slice of Fig. 4-1, with best-fit line superposed to demonstrate validity of linear fit. See Fig. 4-4 for slope and error.

Taking the mean values of k_1 and k_2 within this region, weighted according to

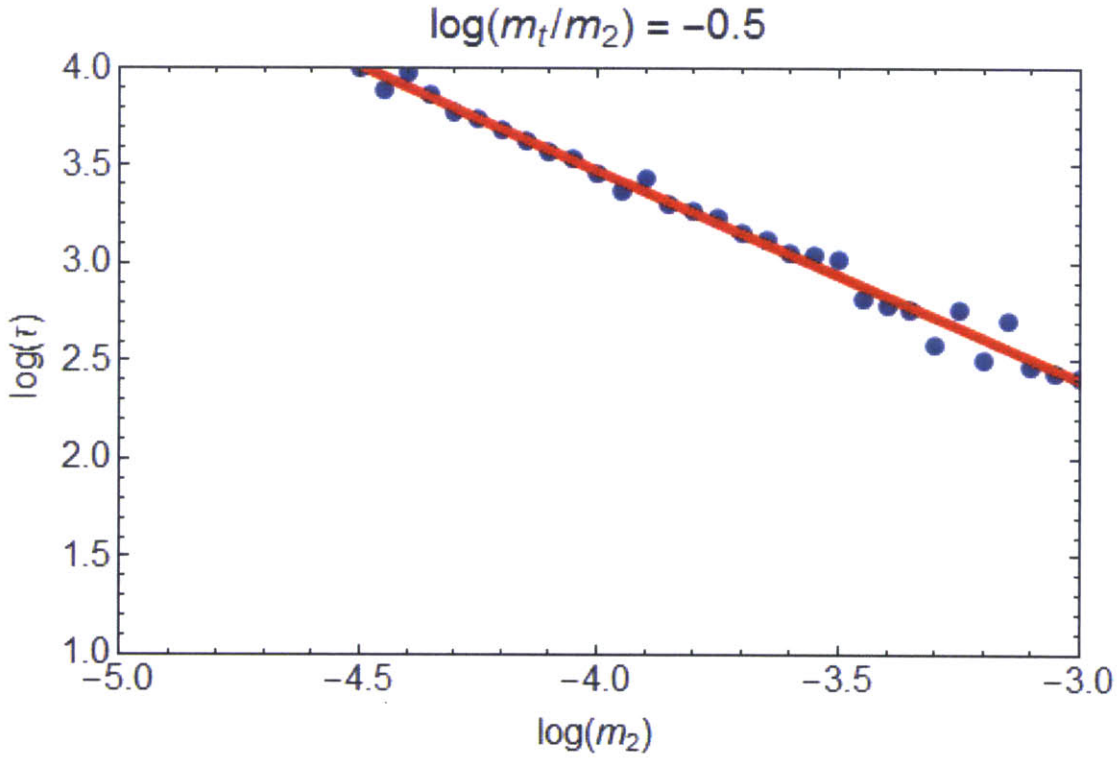

Figure 4-3: A vertical slice of Fig. 4-1, with best-fit line superposed to demonstrate validity of linear fit. See Fig. 4-5 for slope and error.

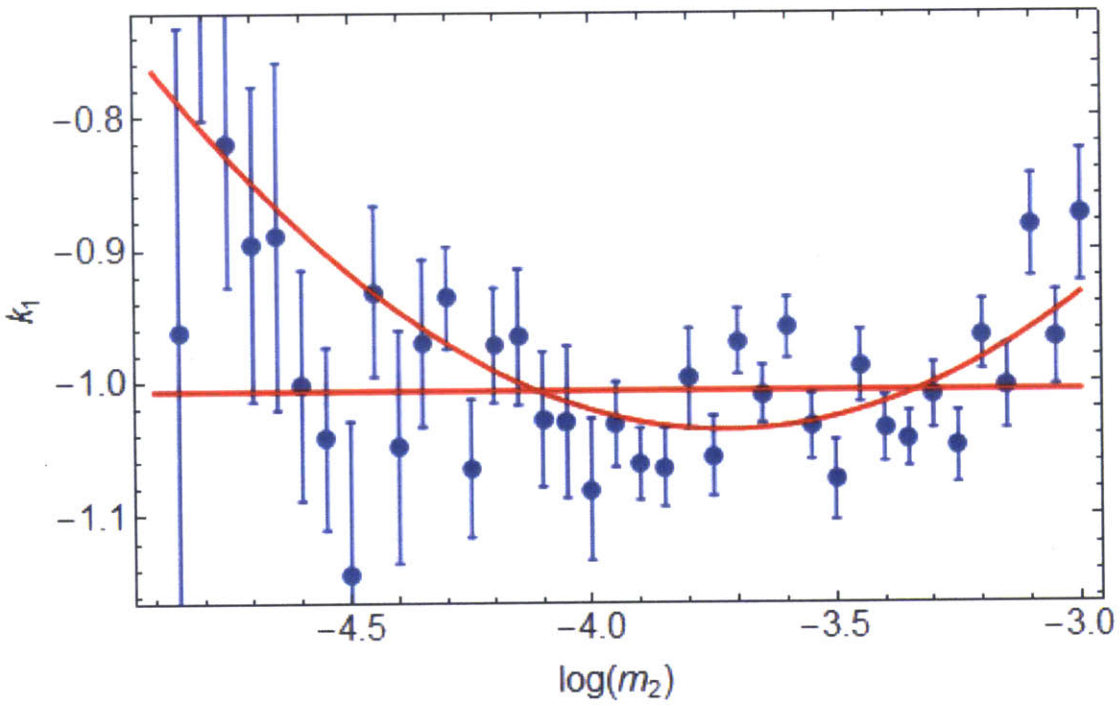

Figure 4-4: The exponent of the power law Eqn. 4.2, determined by fitting lines to vertical slices of Fig. 4-1. Errors are taken from the standard errors of the fits. Plotted in red are a quadratic and a constant function fitted to these points.

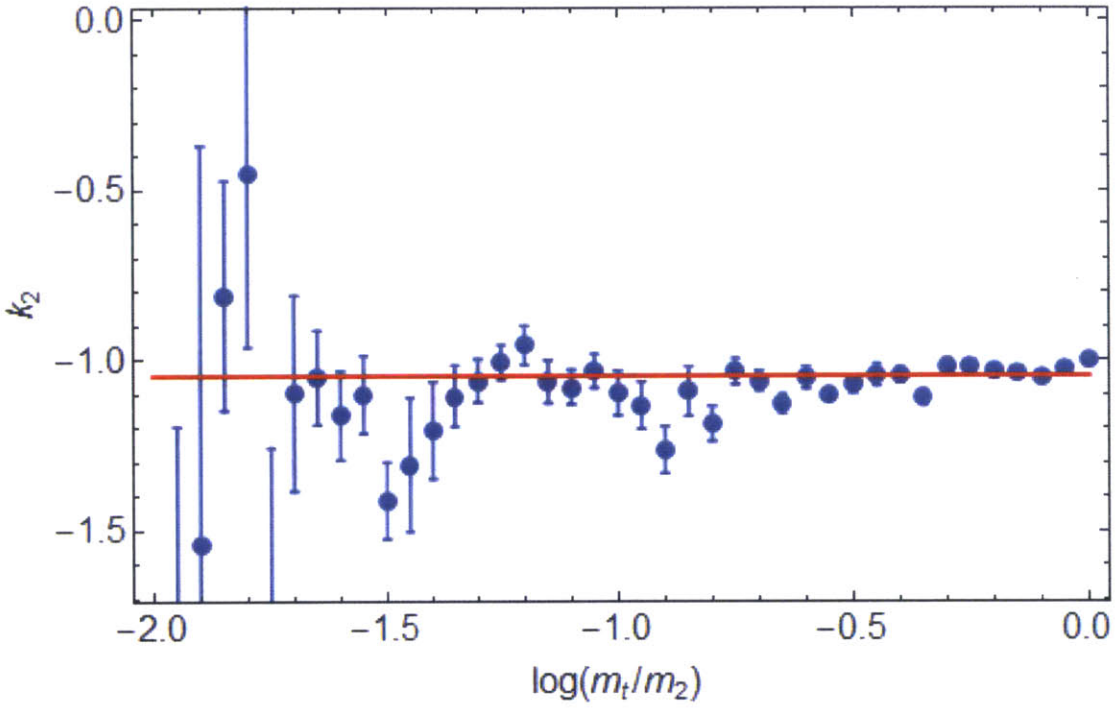

Figure 4-5: The exponent of the power law Eqn. 4.3, determined by fitting lines to horizontal slices of Fig. 4-1. Errors are taken from the standard errors of the fits. Plotted in red is a constant function fitted to these points.

their errors (i.e. taken from the constant fit in each plot), we find that

$$k_{1,avg} = -1.006 \pm 0.006 \tag{4.4}$$

$$k_{2,avg} = -1.047 \pm 0.005 \tag{4.5}$$

In this region, $k_{1,avg}$ does *not* agree with the prediction of Dermott & Murray (1981a) of $-5/3$. This is not a contradiction; the former work was concerned with "horseshoe solutions of the restricted three-body problem in which the particle mass, m_2 [which we call here m_t] is considered to be negligible." Our result is relevant to the region in which $0.01 < m_t/m_2 < 1$, and even though we take $m_2 \leq 0.001$ for the calculation of $k_{1,avg}$, this is evidently not enough to qualify m_t as "negligible."

We now recall that we defined $\mu_t = m_t/m_2$, so assuming, as suggested by Equations 4.4 and 4.5, true values of $k_{1,avg} = k_{2,avg} = 1$, we find that

$$\tau = C\left(m_2^{-1}\left(\frac{m_t}{m_2}\right)^{-1}\right) \tag{4.6}$$

$$\tau = \frac{C}{m_t} \tag{4.7}$$

That is, the horseshoe lifetime—as defined by our stability criterion dependent on width of the horseshoe—is dependent *only* on m_t, to which it is inversely proportional. Observe Figure 4-6, where we perform a grid search in the m_2–m_t plane, rather than in m_2–m_t/m_2, and which corroborates Equation 4.7.

4.2 Conclusions and Discussion

In this work we used the analytic treatment of the stability of Trojan orbits to motivate a numerical exploration of the stability of horseshoe orbits. We set up the problem as a fully general system of differential equations describing the gravitational attractions of a three-body system and used the solutions of this system of equations to determine numerically the lifetimes of horseshoe orbits associated with various masses and initial parameters of the system.

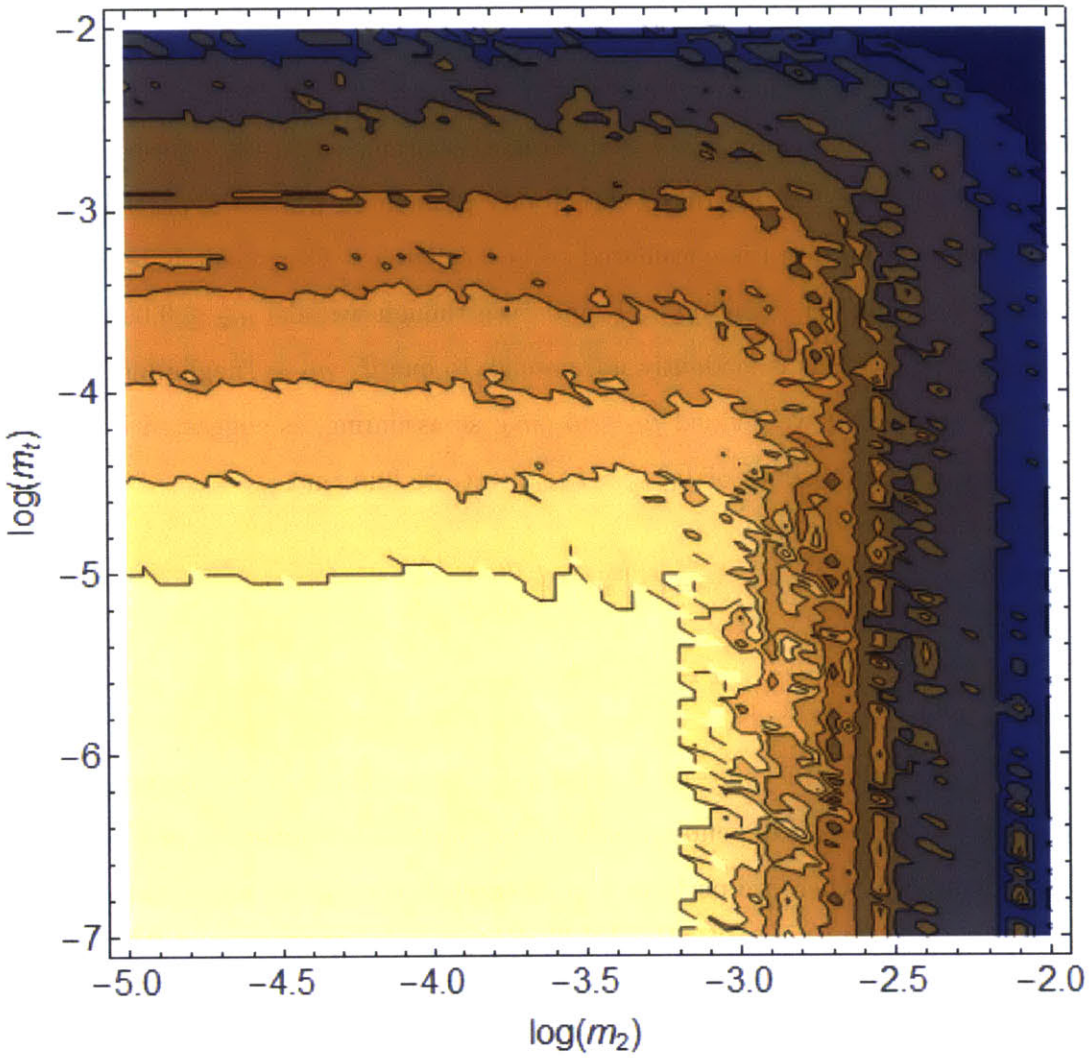

Figure 4-6: A grid search on m_2 and m_t. The beige region indicates lifetimes of $\log \tau \geq 4$, and the contours follow $\Delta \log \tau = 0.5$. The upper-left region agrees with Eqn. 4.7 in that τ does not depend on m_2. The right side of this figure also agrees with the previous grid searches in that τ does not depend on m_t for the less-stable cases where m_2 is large.

After selecting a set of initial positions and velocities expected to admit horseshoe orbits for a wide range of different mass configurations, we then tested horseshoe lifetime based on integrations with mass ratios selected from a grid in the secondary and tertiary masses m_2 and m_t. The result (Figure 3-7) demonstrated a functional dependence of horseshoe lifetime τ on both masses, which could be summarized as a power law (Equations 4.2 and 4.3) on each horizontal and vertical slice of the full grid, rather than a strict mass-ratio cutoff. From these results, we conjectured that the two power laws could be further summarized by a single one: $\tau \propto m_t^{-1}$ (Equation 4.7).

Among our preliminary observations, we found that for very small m_t, stability seems to decrease sharply as $\log m_2$ increases above -3. This is consistent with the critical mass ratio of $m_1/m_2 \approx 1200$ discussed by Ćuk et al. (2012). We confirmed therefore that horseshoe orbits in general impose a stricter condition on the mass ratio m_2/m_1 than do Trojan orbits—true for m_t negligible and even more so as $m_t \to m_2$. If we apply these results to some simple celestial systems, we find the following:

- Many binary-star systems have mass ratios too close to 1 to admit either Trojan or horseshoe orbits.

- Some binary systems, with mass ratios of $m_2/m_1 \lesssim 0.04$ (e.g. an A star of mass $3M_\odot$ with an M star of mass $0.1M_\odot$), could admit Trojan orbits, but not horseshoe orbits.

- In systems like the Solar System, any binary of the $1M_\odot$ star with a planet could admit Trojan orbits (as we know well in the Sun-Jupiter system), while any binary of the star with a body of mass less than Jupiter's could admit both Trojan and horseshoe orbits.

- In this latter category, the third body must be sufficiently small compared to the second body in order to follow a horseshoe orbit—with "sufficiently small" being dependent on the mass of the second body itself, for example according to Figure 4-6.

A shortcoming of our calculation of the average power-law exponents $k_{i,avg}$ was the fact that we should *expect* the functional dependence of τ on m_2 and m_t to vary depending on the region of m_2–m_t space we are concerned with; given that our measurement of $k_{1,avg}$ differed so significantly from Dermott & Murray's (1981a) calculation of $-5/3$, we should expect there to exist truly distinct regimes, e.g. with different power-law exponents. Because, however, we did not know how to demarcate such different regimes—in particular, it was only by inspection that we chose which slices to include in the making of Figures 4-4 and 4-5—we should not necessarily expect a consistent power law throughout the region we did calculate in.

The primary way we could resolve this issue is further-refined grid searches. For example, integrating to longer times (given the computing capacity and time to do so) would reveal portions of the grid for m_2 and m_t even smaller, which would naturally allow us to probe longer-lasting horseshoe orbits and thus explore the entire region more precisely.

We also assumed that no horseshoe orbit, once decayed, would return to a horseshoe shape; it would also be useful to demonstrate this claim more rigorously.

Furthermore, we made the assumption that a particular set of initial positions and velocities would serve to adequately probe all mass combinations. It would be worthwhile to test further the validity of this claim, especially with a more detailed knowledge of horseshoe orbits with lifetimes $\tau > 10000$.

Appendix A

Additional Figures

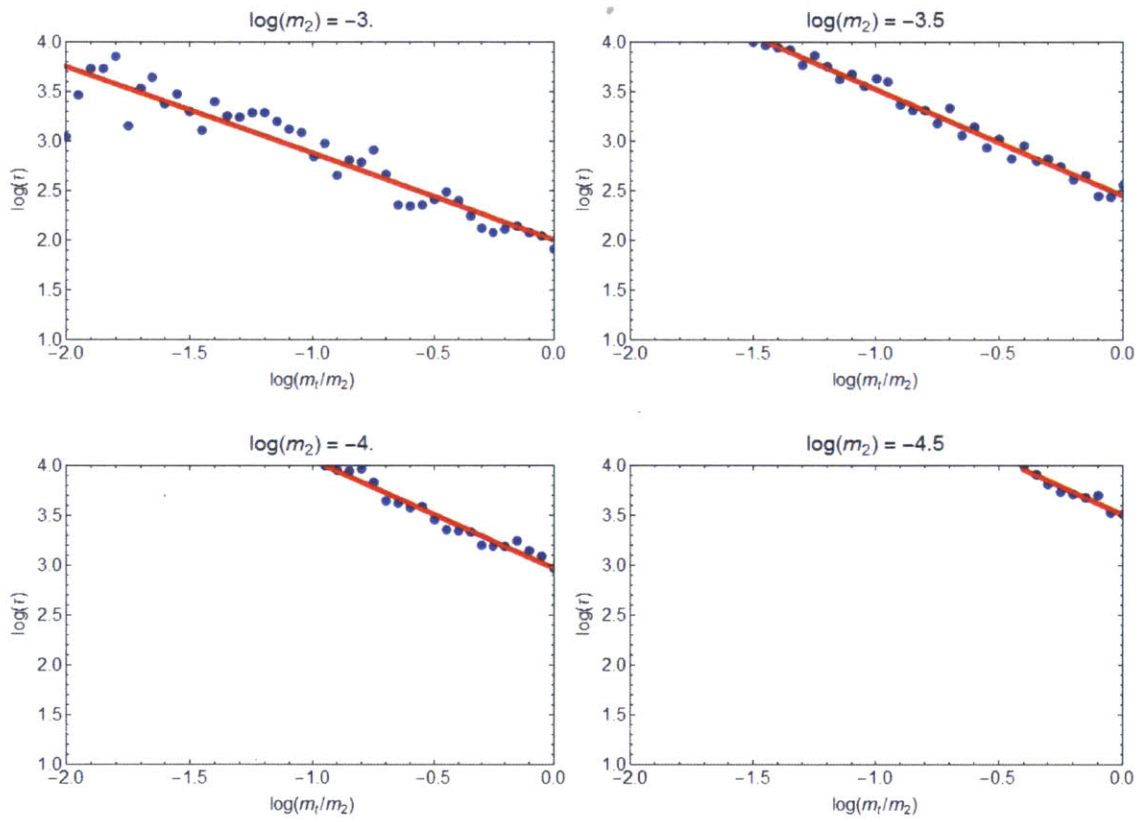

Figure A-1: Four (evenly sampled out of 39) vertical slices of Figure 4-1, for the purpose of calculating k_1 according to Eqn. 4.2, with best-fit lines superposed.

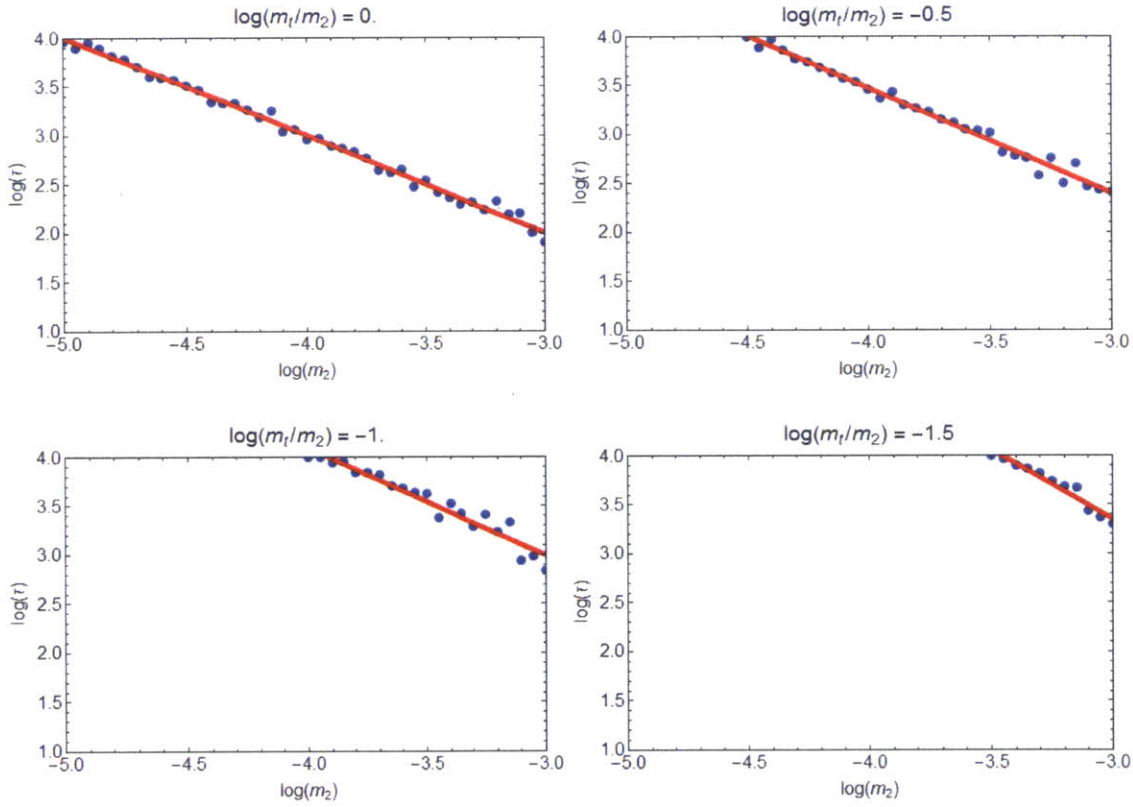

Figure A-2: Four (evenly sampled out of 41) horizontal slices of Figure 4-1, for the purpose of calculating k_2 according to Eqn. 4.3, with best-fit lines superposed.

Bibliography

[1] Christou, A. A., Asher, D. J., MNRAS, 000, 1

[2] Ćuk, M., Hamilton, D. P., Holman, M. J., 2012, MNRAS, 000, 1

[3] Dermott S. F., Murray C. D., 1981, Icar, 48, 1

[4] Dermott S. F., Murray C. D., 1981, Icar, 48, 12

[5] Rappaport, S., 2006, MIT General Doctoral Exam Part II, solutions

[6] Wolfram Research, Inc., 2016, Mathematica, Version 10.4